

Episodic intensification of marine phosphorus burial over the last 80 million years

Received: 3 November 2023

Accepted: 12 August 2024

Published online: 28 August 2024

 Check for updatesJinzhou Peng¹, Dengfeng Li¹✉, Simon W. Poulton², Gary J. O'Sullivan³, David Chew³, Yu Fu¹ & Xiaoming Sun^{1,4}

Marine phosphatization events cause episodic carbonate fluorapatite (CFA) precipitation on seamounts, and are commonly linked to growth hiatuses in ferromanganese (Fe–Mn) crusts. However, the complete record of these events and their paleoenvironmental significance remains poorly understood, in large part due to poor age constraints. Here, we apply U–Pb dating to CFA in Fe–Mn crusts from Western Pacific seamounts. These data exhibit good alignment with Sr isotope ages, revealing six potential phosphatization events. This established CFA chronology tightens the timespan of phosphatization events and refines the age framework of Fe–Mn crusts. We subsequently utilize a multiproxy approach to demonstrate that the phosphatization events occurred coeval with the expansion of oceanic oxygen minimum zones. The Western Pacific Fe–Mn crusts thus document major perturbations in global oceanic phosphorus cycling, which appear to have been driven by climate-induced increases in primary productivity linked to changes in global ocean circulation.

Phosphorus (P) is the dominant limiting nutrient for oceanic primary productivity on geological timescales¹, and thus the long-term bioavailability of P influences atmospheric carbon dioxide levels and climate via changes in organic carbon burial^{2,3}. The P content of the ocean is determined by a balance between the supply of P, which in a well-oxygenated ocean is mostly from continental weathering, and the loss of P via burial in marine sediments^{4,5}. Dissolved oceanic P is dominantly delivered to the sediments in association with organic matter and Fe (oxyhydr)oxide minerals⁶. During diagenesis, however, sink-switching to authigenic phases commonly occurs, with carbonate fluorapatite (CFA) being a major sink for P⁷. CFA often precipitates in the voids or veins of ferromanganese (Fe–Mn) crusts on seamounts^{8,9}, with periods of enhanced CFA precipitation being termed ‘phosphatization events’.

Carbonate fluorapatite in Fe–Mn crusts can provide valuable insight into Cretaceous to modern paleoclimatic conditions, oceanic paleo-redox variability, and P cycle dynamics^{10,11}. In particular, the formation of seamount CFA is considered to be closely linked to the expansion of oxygen minimum zones (OMZs)¹². However, constraints

on the onset and duration of expanded OMZ intervals are currently lacking, and thus an accurate absolute chronometer, such as U–Pb dating of CFA, is crucial to fully utilize the paleoenvironmental information recorded by CFA in Fe–Mn crusts. The oldest oceanic crust (dating back to the early Jurassic¹³) occurs in the Western Pacific (Fig. 1), providing a potential record of multiple intervals of enhanced CFA precipitation.

Phosphatization events are episodic and linked to hiatuses in Fe–Mn crust growth¹⁴, which are widespread across the world's oceans^{8,11}. One common way to detect growth disruptions in Fe–Mn crusts is by comparing their osmium (Os) isotope compositions with the seawater Os isotope curve¹⁵. However, the accuracy of this method is limited due to the low resolution of the seawater Os isotope curve¹⁶. Similarly, the application of strontium (Sr) isotope correlation methods to CFA does not yield absolute ages⁸ and is characterised by time intervals with limited variation in the ⁸⁷Sr/⁸⁶Sr ratio. By contrast, the apatite U–Pb chronometer is a precise dating method with wide-ranging applications in igneous, metamorphic and sedimentary

¹School of Marine Sciences, Guangdong Provincial Key Laboratory of Marine Resources and Coastal Engineering, Sun Yat-sen University, Zhuhai, China.

²School of Earth and Environment, University of Leeds, Leeds, UK. ³Department of Geology, School of Natural Sciences, Trinity College Dublin, Dublin 2, Ireland. ⁴School of Earth Sciences and Engineering, Sun Yat-sen University, Zhuhai, China. ✉ e-mail: lidf3@mail.sysu.edu.cn

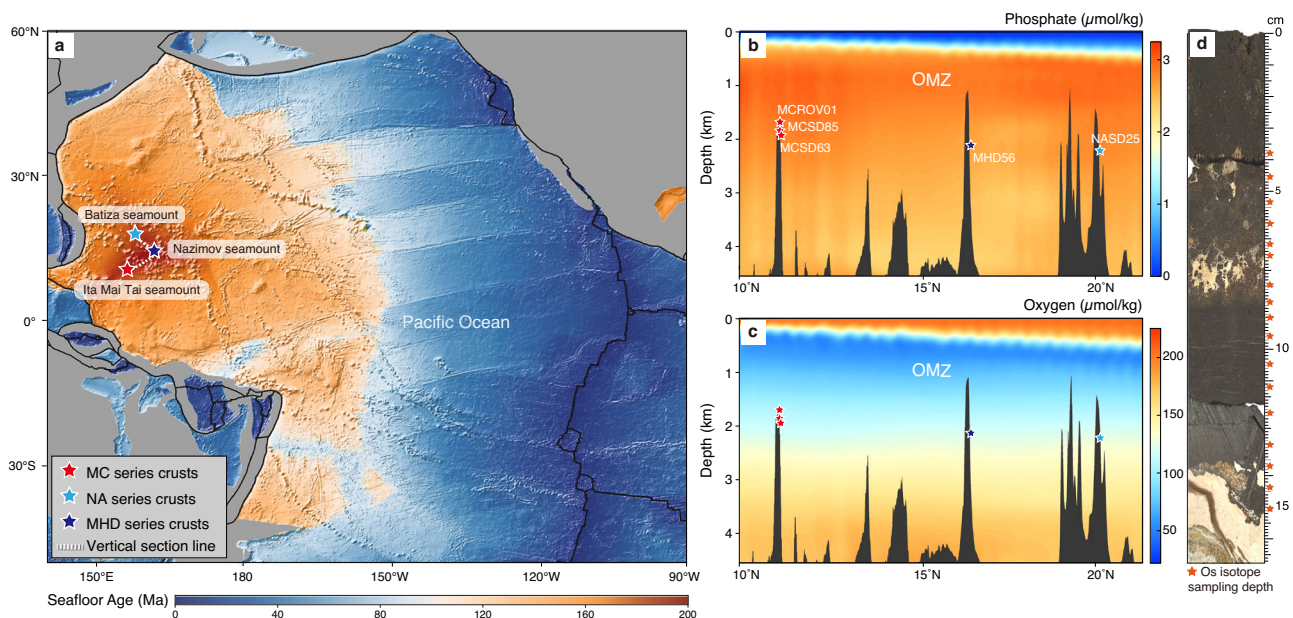


Fig. 1 | Fe–Mn crusts location and regional seawater environment. **a** Fe–Mn crusts located on the seafloor age map. Red, navy blue and light blue stars denote the Fe–Mn crust drill-core locations from the Ita Mai Tai, Nazimov and Batiza seamounts, respectively. The dashed line denotes the locations of present-day vertical phosphate and oxygen profiles generated with Ocean Data View, (Schlitzer,

R., Ocean Data View, odv.awi.de, 2023). Grey areas indicate continents. Map created using open source software Generic Mapping Tools (available at: <http://gmt.soest.hawaii.edu>), and raw data of oceanic crust age from ref. 82. **b, c** Depth-latitude profiles for phosphate and oxygen in the water column. **d** Profile of core MCSDB5, with Os isotope samples depth indicated.

systems¹⁷. Although U–Pb dating of sedimentary apatite is challenging, with some studies yielding U–Pb dates with either poor accuracy or younger than expected ages^{18–20}, other studies have successfully dated CFA grains and bioclastic apatite from sedimentary rocks, yielding ages consistent with independent geological constraints^{21,22}. Thus accurate U–Pb dating of CFA in Fe–Mn crusts would improve constraints on both the timing of phosphatization events and the growth history of Fe–Mn crusts.

In this study, we report in situ U–Pb dating of CFA using laser ablation inductively coupled plasma mass spectrometry (LA-ICP-MS) applied to fifteen samples from five Western Pacific Fe–Mn crusts (Supplementary Data 1; Supplementary Figs. 1 and 2). We utilize these CFA U–Pb ages (independently validated by the Sr isotope chronometer) to more precisely date periods of phosphatization during hiatuses in Fe–Mn crust growth, thus improving their age framework established using Os isotope chronometry. We also employ a variety of additional geochemical data to explore the processes that led to hiatuses in Fe–Mn crust growth and the onset of CFA formation to develop a comprehensive understanding of the environmental controls on oceanic seamount phosphatization events over the last 80 million years.

Results

U–Pb ages of CFA in the Western Pacific Fe–Mn crusts

U–Pb ages (Supplementary Data 2) were obtained from fifteen CFA veinlet/cavity infills, ranging from about 72 to 7 Ma. These ages fall into six distinct time periods that commonly coincide with an increased number of hiatus intervals in pelagic sediments from the Southeast Pacific (Fig. 2). The oldest and youngest of these CFA formation phases occur at 72–71 Ma and 8–7 Ma, respectively, with other intervals of CFA formation occurring at 56–54 Ma, 35–34 Ma, 25–23 Ma, and 11–10 Ma (Supplementary Table 1; Supplementary Fig. 3).

Os isotopic compositions of Fe–Mn crust and in situ Sr isotopic compositions of CFA

The corrected $^{187}\text{Os}/^{188}\text{Os}$ ratios of seventeen successive Fe–Mn oxide samples from the MCSDB5 Fe–Mn crust drill core vary from 0.420 to

0.842, with an average uncertainty of 0.003 (2SE; Supplementary Data 3). The results align with the seawater Os isotope curve from –78 to 7 Ma (Fig. 3). Notably, according to the Os isotope ages and sampling location, distinct hiatuses occurred at –62–54 Ma, 51–42 Ma, 39–33 Ma, and 29–17 Ma.

In situ $^{87}\text{Sr}/^{86}\text{Sr}$ ratios of fifteen CFA samples vary from 0.70762 to 0.70901, with a mean uncertainty of 0.00014 (2SE). Based on the fitting of these results to the global seawater Sr isotope curve, the ages vary from –75.6 to 5.6 Ma (Supplementary Fig. 4). In addition, the Sr isotope ratios of the calcite substrate in core MCSDB5 range from 0.70740 to 0.70755, corresponding to an age older than 78 Ma.

Discussion

Utilising CFA for precise dating of Fe–Mn crusts

Uranium–Pb CFA ages hold potential as an indicator for growth interruptions in Fe–Mn crusts¹⁴, because individual CFA crystals have a well-defined euhedral morphology suggestive of an authigenic origin (Supplementary Fig. 5). In addition, CFA aggregates form as an integrated part of the stratigraphy of Fe–Mn crusts, precipitating as a cement in sediment pores and void spaces of the surface Fe–Mn crust during phosphatization events⁸. CFA can also replace pre-existing calcite in the pores, which is rapidly dissolved in the presence of phosphate²³. This contributes to an elevated Ca/Mg ratio, thereby promoting the crystallization of CFA²⁴, and the foraminiferal residues in the CFA of core MCSDB5-6 are a result of calcite dissolution and subsequent CFA precipitation¹¹ (Supplementary Fig. 2b). Furthermore, the REE distribution patterns of CFA mimic that of seawater (Supplementary Fig. 6), indicating direct precipitation from seawater²⁵, while the absence of Eu anomalies in the CFA REE spectra argues against late-stage alteration by hydrothermal fluids²⁶.

Here, each of the fifteen CFA samples defines a robust discordia regression line in Tera–Wasserburg plots (Supplementary Fig. 3), with no evidence of loss or gain of U and Pb²⁷. The CFA initial $^{207}\text{Pb}/^{206}\text{Pb}$ ratios derived from an unanchored Tera–Wasserburg upper intercept (0.829–0.849) differ slightly from the Stacey and Kramers two-stage crustal Pb evolution model²⁸, but are within the $^{207}\text{Pb}/^{206}\text{Pb}$ range of the

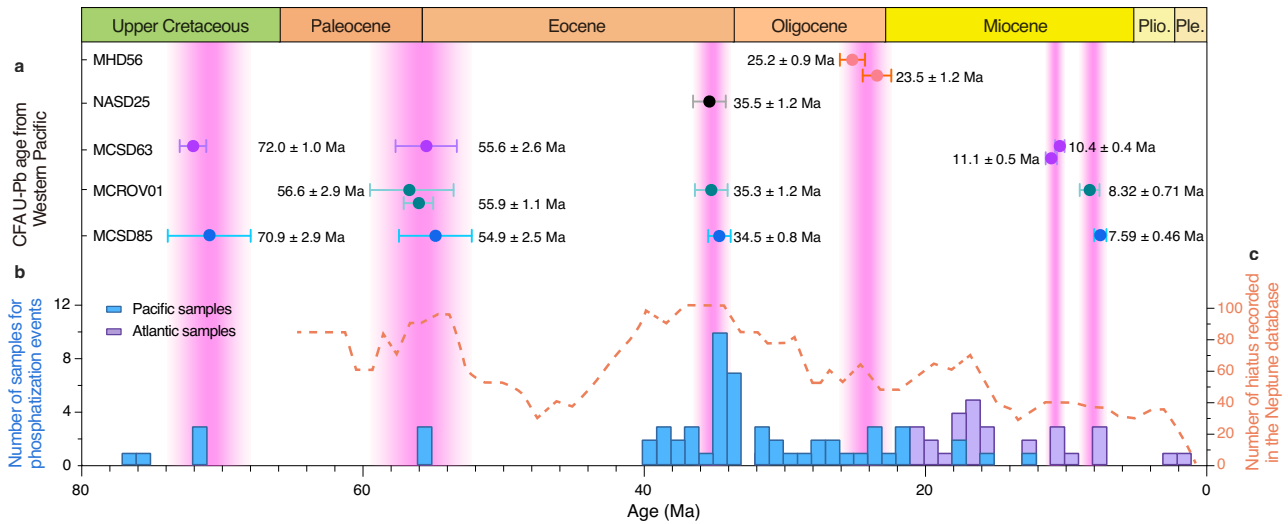


Fig. 2 | Comparison of carbonate fluorapatite (CFA) U-Pb ages to previous phosphatization event periods and sedimentary hiatus over the past 80 million years. **a** Tera-Wasserburg lower intercept ages for fifteen CFA samples from the five Fe–Mn crusts. Age uncertainties are presented at the 2σ confidence level. The ages are divided into six periods, with the magenta shading representing the CFA formation time range for each period. **b** Histograms of phosphatization

ages in the Pacific and Atlantic, as identified by $^{87}\text{Sr}/^{86}\text{Sr}$ chemostratigraphic correlation. Published age data for the Pacific and Atlantic are from refs. 8,11,15,37 and refs. 11,14, respectively. **c** The number of hiatuses identified in the Southwest Pacific sediment cores (orange dashed line)⁸³. Source data are provided as a Source data file.

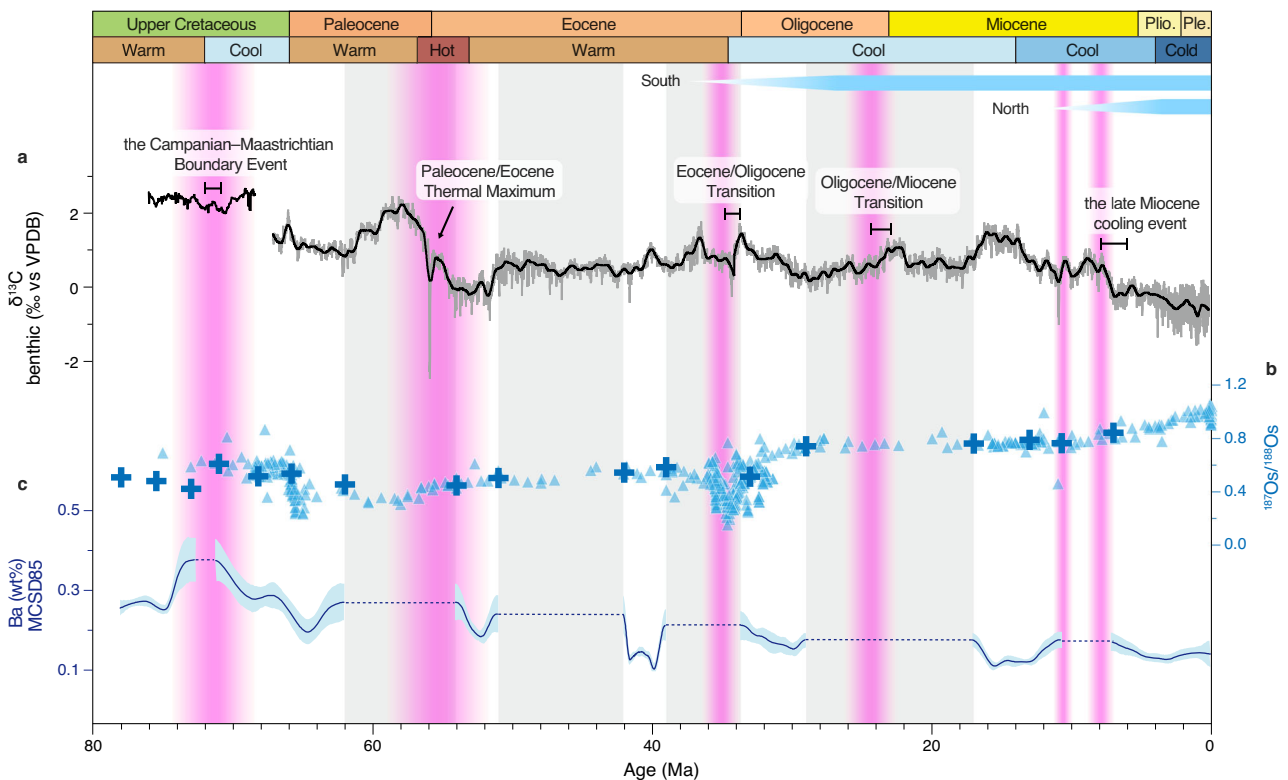


Fig. 3 | Comparison of paleoclimate and ocean chemistry changes with geochemical data for the MCSD85 Fe–Mn crust over the past 80 million years. Graded blue arrows represent ice sheet expansion stages in the northern and southern hemispheres, and climate classification is from ref. 84. Grey shading denotes intervals of crustal growth interruption, as determined by the Os isotope chemostratigraphic correlation and previous studies in the Western Pacific. Magenta shading denotes the phosphatization phases identified in this study. **a** Benthic foraminiferal $\delta^{13}\text{C}$ record during the Cenozoic⁸⁴ and $\delta^{13}\text{C}$ stratigraphy for

the Upper Campanian–Maastrichtian⁸⁵. The black line represents the lowest fit curve from the grey measure data. **b** Comparison between Os isotope data from the MCSD85 Fe–Mn crust (blue crosses) and the seawater $^{187}\text{Os}/^{188}\text{Os}$ curve (light blue triangles). **c** Ba contents (lowest fit) in Fe–Mn crust MCSD85, where the light blue shading denotes the 90% confidence interval based on a lowest fit. Dashed lines indicate no data during the hiatus intervals. Source data are provided as a Source data file.

deep ocean²⁹. Eleven of the 15 samples yield initial $^{207}\text{Pb}/^{206}\text{Pb}$ ratios consistent with the $^{207}\text{Pb}/^{206}\text{Pb}$ ratios derived from analyses of texturally adjacent Fe–Mn oxides (Supplementary Discussion); the Pb isotopic values of adjacent Fe–Mn oxides were used to anchor the CFA $^{207}\text{Pb}/^{206}\text{Pb}$ ratios for the intercept age calculation (Supplementary Data 2).

Positive correlation between U and Ca in CFA samples (Supplementary Fig. 7) implies that U was incorporated into CFA during formation, rather than being subsequently adsorbed, suggesting that the CFA U–Pb chronometry represents the timing of crystallization. Although the Sr isotope ages have a large uncertainty, the good consistency between the CFA U–Pb ages and their Sr isotope ages (which also correlate well with CFA Sr isotope dates from the Western Pacific and Atlantic seamounts) further demonstrates the reliability of the obtained U–Pb ages^{8,30} (Supplementary Figs. 4 and 8).

Closed system behaviour is a prerequisite for U–Pb dating²⁷, and U–Pb system closure in sedimentary phosphates is thought to be associated with the cessation of CFA-porewater interactions¹⁹, with sediment lithification during burial diagenesis potentially being a significant cause²¹. Many sedimentary apatite ages therefore record geological processes that drove the closure of the U–Pb system³¹. For CFA from different settings, crystal morphology may play an important role. The rounded and elongated CFA crystallites that make up peloids on continental margins have high reactivity and significant inter-crystalline porosity³¹. Following formation in surficial sediments they can undergo winnowing, current scouring and then burial, during which they may experience alteration or resetting³². By contrast, authigenic euhedral CFA crystals within Fe–Mn crusts are larger, tightly stacked and have lower porosity than CFA on continental margins⁹ (Supplementary Fig. 5). The CFA is then cemented by Fe–Mn crusts that terminate the interaction with porewater/seawater. Additionally, hydrogenetic Fe–Mn crusts are typically not overlain by sediment, and the CFA within Fe–Mn crusts does not undergo significant late-stage diagenesis. As a result, there are significant differences between the diagenesis and morphology of CFA in Fe–Mn crusts and CFA on continental margins, that could explain their differing U–Pb systematics.

Strontium isotope dating is a relative chronometer, where the ages are obtained by matching the Sr isotope ratio of CFA to the seawater Sr isotope curve. There are two major limitations when employing Sr isotope dating to CFA in Fe–Mn crusts: (1) The Sr isotope method only provides a relative age, the accuracy of which is controlled by the accuracy of the Sr isotope analyses and uncertainties in fitting the Sr isotope data to the seawater Sr isotope curve; (2) The seawater Sr isotope curve is relatively non-variant, with a range of only 0.0016 over the last ~80 million years³³. In particular, from ~75–35 Ma, Sr isotope ratios are almost constant, leading to multiple potential ages with large uncertainties⁸, even before considering possible sample contamination issues and the accuracy of measurements. In order to obtain better age constraints, it has been suggested that age-depth models and their associated age uncertainties should be established by applying two or more chronology methods³⁴. By contrast, U–Pb dating has two main advantages: (1) U–Pb ages provide absolute dates reflecting the timing of CFA formation; (2) the U–Pb system simultaneously determines two individual sets of radioisotope systems (^{238}U to ^{206}Pb and ^{235}U to ^{207}Pb), and these two isotope clocks are calibrated against each other^{27,35}. The half-lives of 4468 and 704 Ma for ^{238}U and ^{235}U , respectively, make it possible to date CFA of any age, although for Mesozoic and younger samples, only the $^{206}\text{Pb}/^{238}\text{U}$ ratio can be practically used to obtain precise ages³⁶. As a result, if U–Pb dating can be successfully applied to CFA, it promises to refine further the timing of phosphatization events and their temporal and spatial distributions.

Carbonate fluorapatite occurs as part of the growth sequence in Fe–Mn crusts, so our measured U–Pb ages represent the maximum age of the crust below, and the minimum age of the crust above. We utilize

Os isotope chronology to first determine growth interruptions in the MCS85 Fe–Mn crust, yielding growth interruption durations of ~6 Ma (39–33 Ma) and ~12 Ma (29–17 Ma) (Fig. 3). These age ranges are considerably refined by our U–Pb dating, giving smaller hiatuses of 3.0 Ma (36.7–33.7 Ma) and 3.8 Ma (26.1–22.3 Ma), respectively. In addition, the U–Pb dating reveals phases of CFA formation at ~72–71 Ma, 11–10 Ma and 8–7 Ma that are not identified by Os isotope dating. The CFA U–Pb absolute dating thus yields better constrained (and shorter) durations for hiatuses in Fe–Mn crust growth.

Previous work on Western and Central Pacific seamount phosphorites has documented two major phosphatization intervals, occurring in the late Eocene/early Oligocene (39–34 Ma, peak at 35 Ma) and late Oligocene/early Miocene (27–21 Ma, peak at 25 Ma), in addition to some minor events occurring at ~71 Ma, 55 Ma, 31 Ma and 15 Ma^{8,37} (Fig. 2). These events are similar to those that occurred in continental margin settings, which also have a similar discrete record of CFA growth³². The record also suggests near-persistent minor phosphatization throughout the ~40–21 Ma interval. However, there remains an absence of compelling evidence to substantiate a prolonged phosphatization event in the Pacific Ocean at this time, and instead this interval of apparent phosphatization may reflect the limited resolution offered by Sr isotopic chronology. This difficulty in identifying discrete phosphatization events using Sr isotope chemostratigraphic correlation makes it difficult to establish environmental drivers for the phosphatization events.

Four of the phosphatization events we identify have previously been documented in the Pacific (based on three or more occurrences), but there are two events we document during the late Miocene (ca. 11–10 Ma and 8–7 Ma) that have only previously been reported from Atlantic seamounts¹¹. The more limited occurrence of late Eocene to early Miocene phosphatization events in our Pacific record relative to previous records, is potentially attributable to the limitations in Sr isotope dating discussed above, and/or sampling limitations. With regards to the latter, previous analyses of CFA have been widely distributed, encompassing different water depths in the Western, Central and Northwestern Pacific, as well as in the Atlantic. Thus, although there are potential sampling biases, our approach demonstrates the potential for CFA U–Pb geochronology to accurately define the timing of phosphatization events in the global ocean.

Drivers of phosphatization events

Our identification of six discrete phosphatization events across a wide temporal range provides an ideal opportunity to gain insights into the causative mechanisms behind phosphatization events. Laboratory experiments have shown that the chemical reactions that generate CFA crystals (approximate formula $\text{Ca}_5(\text{PO}_4)_3\text{F}$) result from an increase in Ca^{2+} and phosphate concentrations in seawater²⁴. In upwelling regions such as continental margins and seamounts, increased phosphate concentrations promote the formation of calcium phosphate precursor phase(s), which is an important prerequisite for CFA precipitation²³. In addition, the depth of OMZs and the degree of anoxia have been shown to be intimately connected to the growth of Fe–Mn crusts³⁸. The low oxygen conditions in the OMZs then inhibit further precipitation of Fe–Mn oxides³⁹, and promote partial dissolution of pre-existing Fe and Mn oxides, releasing adsorbed P and thus further favouring local enrichment of phosphate⁴⁰. Therefore, phosphatization events have been attributed to the downward expansion of OMZs, representing settings that are characterized by abundant bioavailable phosphorus⁴¹ (see Fig. 1 for dissolved P and O_2 concentrations in the modern ocean), thereby creating suboxic-anoxic conditions where the OMZs intersect the seamounts.

Existing marine climate models struggle to predict the intensity and extent of OMZs⁴². The global deoxygenation trend observed over the past 50 years has been attributed to a warming climate leading to a reduction in the oceanic dissolved oxygen levels⁴³. However, nitrogen

isotope studies indicate that on long-term timescales, the spatial extent of OMZs is contracted during warm periods (e.g., the Middle Miocene Climatic Optimum)⁴⁴. Here, we note that reconstructed paleoclimate temperatures, including sea surface temperatures (SST) derived from Tex₈₆ and $\delta^{18}\text{O}$ isotopes in foraminifera do not display any clear relationship with the six identified phosphatization intervals, which instead occur across a wide range of climatic conditions (Supplementary Fig. 9). Eolian inputs and sea level change (which may indirectly affect the extent and intensity of OMZs by influencing oceanic ventilation and water mass exchange^{45,46}), also display no clear relationship with the phosphatization events. Hence, these factors do not appear to have been the fundamental drivers of expanded OMZs during phosphatization events.

Ocean primary productivity, by contrast, is likely to have been a major contributor to the expansion of OMZs in seamount regions, with high productivity driven by enhanced nutrient availability increasing biological oxygen consumption in the water column⁴⁷. Barium (Ba) in deep-sea sediments is a potentially useful proxy for paleo-ocean productivity⁴⁸, and its concentration in Fe–Mn crusts (by adsorption) is commonly positively correlated with the degree of primary productivity⁴⁹. Here, the coupling of phosphatization events with broad intervals of high Ba concentrations in crust MCSD85 (Fig. 3) supports enhanced productivity during phosphatization events. Moreover, vanadium, which is commonly enriched in sediments deposited under anoxic conditions⁵⁰, is strongly correlated with Ba in crust MCSD85 (Supplementary Fig. 10), suggesting that suboxic-anoxic conditions were initiated by enhanced productivity in the water column. Hence, increased oceanic primary productivity appears to have caused the episodic expansion of OMZs, thereby driving the phosphatization events.

Phosphate sources for phosphatization events

Riverine P provides the main oceanic P source, with less than a third of the total riverine P flux occurring in a potentially reactive form⁵¹. Aeolian-sourced P in dust, although comprising less than 10% of the total P flux, also constitutes a significant source in the open ocean, including distal seamounts⁵². Another important source of dissolved P in the deep sea is from the remineralization of organic matter, which may occur in the water column, at the sediment–water interface, or upon burial⁷. The P inventory of the open ocean is dominated by dissolved species, more than 95% of which accumulate in the deep ocean⁶. In addition, an increase in dissolved P concentrations occurs in older deep waters due to the continuous accumulation of sinking particulate matter and its regeneration⁵³. Thus, dissolved P concentrations are higher in deep Pacific water relative to deep Atlantic water because North Atlantic deep water ultimately flows into the North Pacific⁵³. This suggests that changes in ocean circulation patterns and subsequent redistribution of P between ocean basins may significantly alter global oceanic P concentrations⁵⁴. Indeed, the seamount phosphatization events we identify occur under distinct climatic transitions between both warmer and cooler temperatures (see Fig. 3, where the benthic $\delta^{13}\text{C}$ profile is shown for context), suggesting that changes in oceanic circulation during climate transitions may have resulted in the redistribution of P between different ocean basins, which we explore further below.

Most ancient sedimentary phosphate deposits on continental margins coincided with high surface primary productivity caused by intensified upwelling⁴. Upwelling delivers deep P-rich waters to shallow shelves, where primary productivity results in P uptake into organic matter and subsequent conversion to apatite in the accumulating organic-rich sediment^{4,55}. This process is evident in modern settings such as the Peru shelf, where phosphorite formation occurs as a consequence of coastal upwelling and limited dilution by land-based sedimentation⁵⁶. Similarly, seamounts act as natural barriers to currents, driving local upwelling often accompanied by current

acceleration⁵⁷, thereby enhancing primary productivity in seamount regions. While upwelling is of fundamental importance, changes in continental weathering and shelf area expansion have also facilitated the CFA deposition in ancient and modern continental margin settings to a certain extent³². The phosphorus sources for seamounts in the open ocean are less directly impacted by sea-level fluctuations, with aeolian dust potentially playing a critical role.

The third phosphatization interval at ~35–34 Ma is a particularly important event³⁰. This event is aligned with global cooling during the Eocene–Oligocene Transition (EOT; ~34 Ma; Fig. 3), and thereby serves as a broader case study for phosphatization events during intervals of cooling. Global cooling associated with the expansion of the Antarctic ice sheet generated Antarctic Bottom Water, which enhances deep water circulation to the north⁵⁸. Antarctic Bottom Water transports nutrients into the Pacific basin, facilitating increased upwelling and primary productivity in the vicinity of seamounts⁵⁹. Similar changes in circulation during intervals of cooling occurred at about 72–71 Ma, 25–23 Ma and 11–10 Ma, which could have facilitated similarly enhanced nutrient transfer between deep-sea basins^{60–64}.

The previously unrecognized late Miocene–early Pliocene (~8–7 Ma) Pacific phosphatization episode appears temporally coincident with a ‘biogenic bloom’ event that occurred during late Miocene cooling⁶⁵. Increased surface primary productivity in the open ocean and the expansion of OMZs occurred across near-equatorial and upwelling regions^{66,67}, and the enhancement of late Miocene circulation again facilitated nutrient transport between different ocean basins, augmenting primary productivity in the divergence zone⁶⁸. Therefore, the enhancement of ocean circulation and consequent transfer of phosphate between different ocean basins during intervals of cooling appears to have been an important trigger for phosphatization events. Furthermore, this event has been attributed to the intensification of the Asian monsoon at ~8 Ma⁶⁹. Enhanced physical weathering and transport of eolian dust commonly increased the supply of micro-nutrients to the Pacific during cooling intervals, thereby elevating surface ocean productivity⁷⁰. While this is unlikely to have been the major factor driving all phosphatization events, it may help to explain why phosphatization events were more widespread in the Pacific.

By contrast, the phosphatization event at ~56–54 Ma (Fig. 3) occurred during an interval of warming (the Paleocene–Eocene Thermal Maximum; PETM). Across this interval, high atmospheric CO₂ concentrations helped to amplify continental weathering, resulting in an increased flux of bioavailable P to the ocean⁷¹. There was a massive increase in the intensity of the marine biological pump (“productivity feedback”), which is thought to have been a possible recovery mechanism from this extreme thermal event⁷². A strong shift in deep-sea circulation at the onset of the PETM led to a change from Southern Hemisphere overturning to Northern Hemisphere overturning⁷³, resulting in intense bottom currents and upwelling in the Pacific. This process has been proposed to explain the formation of phosphorite deposits on the southern Tethyan margin during the PETM⁷⁴. In addition, prevalent bottom and intermediate water column deoxygenation during the PETM enhanced phosphorus recycling from sediments back to the water column, promoting increased biological productivity and expanding OMZs under the influence of ocean circulation in seamount regions⁷⁵.

This discussion highlights that seamount phosphatization events occurred during both cold and warm transitional periods, where changes in ocean circulation drove phosphorus transport between ocean basins. Consequently, localized upwelling at seamounts transports phosphate directly up the seamount flanks or summits where Fe–Mn crusts are located, and additionally transfers nutrients to the sea surface to elevate primary productivity. This causes expanded OMZs along with high P availability, resulting in ideal conditions for CFA formation. We thus propose that phosphatization events on

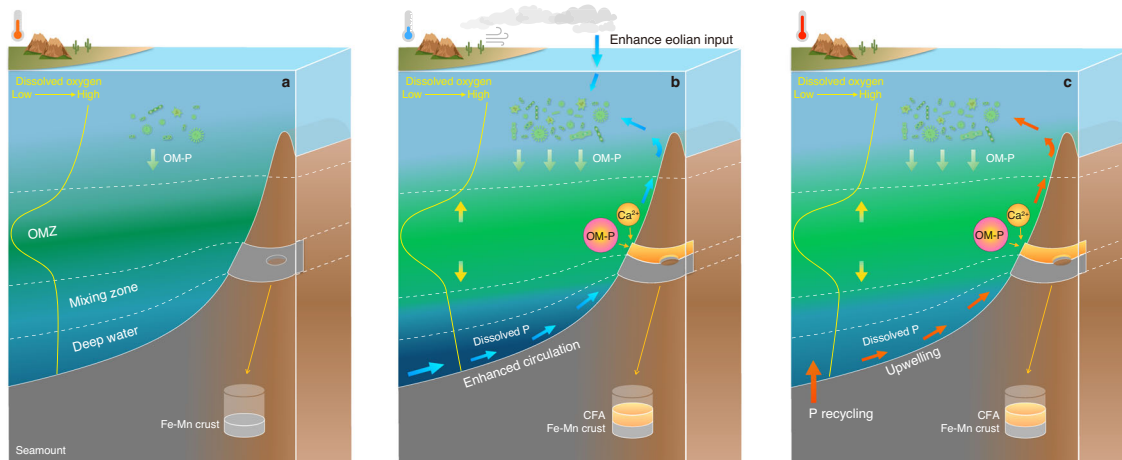


Fig. 4 | Schematic diagram for the onset of phosphatization events on seamounts. a In the mixing zone between the oxygen minimum zone (OMZ) and oxygen-rich bottom water, Fe–Mn oxides precipitate under oxic conditions to form unphosphatized Fe–Mn crusts. **b** During periods of cooling, enhanced circulation/upwelling and eolian inputs lead to strengthened primary productivity, providing increased organic matter-bound phosphorus (OM-P) and a downward expansion of

the OMZ, which promotes phosphatization events on seamounts. **c** During warming, seamount upwelling from ocean circulation and recycling of P from the suboxic-anoxic seafloor promotes enhanced primary productivity, contributing to the expansion of the OMZ and the development of seamount phosphatization events.

seamounts occurred via the following mechanisms during periods of climate transition: (1) OMZs were spatially limited when primary productivity was relatively weak. On seamount flanks, Fe–Mn oxides precipitated to form Fe–Mn crusts in the mixing zone between the OMZs and bottom currents (Fig. 4a); (2) During cool intervals, enhanced circulation and local upwelling brought nutrients to the ocean surface, increasing primary productivity and the depositional flux of organic P, with eolian dust inputs of nutrients potentially augmenting this process (Fig. 4b). During warm intervals, a shift in ocean circulation increased primary productivity, and the prevalent development of suboxic-anoxic conditions in bottom waters promoted P remineralization and recycling back into the water column, further enhancing dissolved P concentrations (Fig. 4c). These perturbations during intervals of climate cooling and warming facilitated the downward expansion of OMZs to encroach upon Fe–Mn crusts, promoting phosphatization. Considering that the expansion of the circulation-controlled open-ocean OMZs does not initiate or end instantaneously⁴⁴, the formation of CFA represents a gradual shift or enhancement in circulation during phosphatization events.

Our approach demonstrates that CFA within Fe–Mn crusts is highly amenable to U–Pb dating, and is compatible with Os isotope and Sr isotope chronometric constraints on Fe–Mn crust and CFA respectively, while CFA micro-textural and -structural observations show consistent patterns between Fe–Mn crust growth zones of similar age derived from the U–Pb dating of adjacent CFA cements (Supplementary Discussion). Therefore, U–Pb dating of CFA provides precise and accurate age constraints on phosphatization events, enabling growth hiatuses in Fe–Mn crusts to be more precisely ascertained and complementing the age framework determined via the Os isotope chronometer. Our precise U–Pb dating refines the timeline of phosphatization events from the late Cretaceous to the present, delineating more constrained spans than previously recognized, with events occurring during both cool and warm intervals. During cool intervals, increased oceanic primary productivity and the expansion of OMZs were likely driven by enhanced deep-sea circulation and upwelling in the vicinity of seamounts along with eolian dust input. During warmer intervals, enhanced productivity and expanded OMZs likely occurred due to changes in ocean circulation and efficient P cycling from sediments deposited under suboxic-anoxic bottom

water conditions. Hence, we conclude that U–Pb dating of CFA in Fe–Mn crusts has major potential for reconstructing perturbations to the oceanic P cycle.

Methods

Os isotope analyses

A total of 17 micro-drilled Fe–Mn oxide samples were taken from core MCS85 (while carefully avoiding CFA), with a ~2 mm layer thickness and a powder weight of ~2 g per sample. The analyses of Os contents and isotopic compositions were conducted using N-TIMS (negative thermal ionization mass spectrometry) at the State Key Laboratory of Isotope Geochemistry (Guangzhou Institute of Geochemistry, Chinese Academy of Sciences), following procedures⁷⁶: (1) Sample powder (0.5–1 g) was digested in Carius tubes, and appropriate amounts of the individual ¹⁸⁵Re and ¹⁹⁰Os spike solutions were weighed and added; (2) The tubes were chilled in a liquid N₂ and ethanol bath, and 2.5 ml of concentrated HCl and 7.5 ml of concentrated HNO₃ were successively added. The Carius tubes were then sealed, steel jacketed, and heated in an oven at 230 °C for 24 h; (3) After decomposition, the glass tubes were again chilled in a liquid N₂ and ethanol bath before opening. After thawing, the contents were poured into 20 ml centrifuge tubes to allow precipitation of the residual solids; (4) The supernatant solutions were transferred into 30 ml PFA (Perfluoroalkoxy) vials and subjected to Os solvent extraction by CCl₄, followed by back-extraction into concentrated HBr⁷⁷; (5) The extracted Os fraction was further purified by micro-distillation prior to N-TIMS analysis. Osmium was loaded in HBr on 99.999% Pt filaments (H. Cross Company, USA), and Ba(OH)₂ emitter solution was loaded on top of the sample to enhance ion emission. Os isotope compositions were measured in pulse-ion counting electron multiplier mode. The results are listed in Supplementary Data 3.

Trace elements and U–Pb dating of CFA using LA-ICP-MS

Trace element analyses were conducted at the Key Laboratory of Marine Resources and Coastal Engineering, SYSU, using an Agilent 7900 ICP-MS coupled to a 193 nm Coherent GeolasPro laser. For trace element concentrations in the Fe–Mn crusts and CFA, single spot ablations were performed with a 32–60 μm beam size, 5 J/cm² fluence, and a 5 Hz repetition rate. The trace element compositions of Fe–Mn

crusts were calibrated against the GSE-IG, NIST 610 and 612 standards, using Ti (EPMA data; Supplementary Data 4) as the internal elemental standard, while trace element analysis of CFA used P as the internal elemental standard. Trace element analyses of the crust and CFA were conducted separately to enhance the experimental precision, and the data for the CFA and Fe–Mn crusts are provided in Supplementary Data 5.

The U–Pb dating approach employed a line scan (raster) mode in order to obtain smoother signals and less downhole fractionation. To avoid Pb contamination and to improve the accuracy and precision of the U–Pb results, we pre-ablated the region of interest to be dated to remove material on the sample surface. A large spot size of 160 μm was used to maximise the signal intensity, and the analyses employed a 5 J/cm² laser fluence, 5 Hz repetition rate, and a 2 $\mu\text{m/s}$ scan speed. In order to ensure the reliability of the ²⁰⁶Pb/²³⁸U ratio, the oxide ratio in the plasma (as measured by ThO/Th) was limited to <0.5%. An internal smoothing device was employed throughout the experiments to ensure signal stability. Madagascar apatite 2 (MAD2; age = 474.25 ± 0.41 Ma) was used as the primary age reference material, with the Durango and McClure apatite used as secondary age reference materials⁷⁸, with each analysis comprising a 20 s background measurement and a 45 s data acquisition (Supplementary Data 6).

Data reduction for U–Pb dating was conducted with Iolite 4.8.1 using the VizualAge_UcompPb data reduction scheme⁷⁹, which can account for variable common Pb in the primary apatite U–Pb age reference materials. The data reduction scheme first applies a common Pb correction to the user-selected age standard integrations, and then fits session-wide “model” U–Pb fractionation bias to the time-resolved U–Pb standard data. The final result output style is based on the PLASMAge recommendations (<http://www.plasmage.org/recommendations/home.html>). The U–Pb results, including the common Pb content (*f*_{206c}), were formatted using *PlasmaAge.py* code from GitHub (<https://github.com/iolite-LA-ICP-MS/iolite4-python-examples>). The IsoplotR software⁸⁰ was used to construct the concordia/intercept diagram, isochrons, and for weighted mean age and uncertainty calculations. The ²⁰⁷Pb/²⁰⁶Pb initial ratios used to anchor the CFA U–Pb intercepts were obtained by Pb isotopic analysis of texturally adjacent Fe–Mn oxides (Supplementary Fig. 3; Supplementary Data 2).

LA-MC-ICP-MS strontium isotopic analysis

Strontium isotopic ratios of CFA were analyzed using laser ablation multi-collector inductively coupled plasma mass spectrometry (LA-MC-ICP-MS). The laser system used was an Australian Scientific Instruments RESOLUTION LR coupled with a Nu Instruments Nu Plasma II MC-ICP-MS (Supplementary Data 6). A 193 nm ArF excimer laser was employed at a fluence of 4.5 J/cm². Each measurement consisted of a 20 s background signal (gas blank) followed by a 40 s line scan using a 90 μm laser beam diameter at an 8 Hz repetition rate. Helium at a flow rate of 370 ml/min served as the carrier gas, which was mixed with argon (–0.97 L/min) via a T-connector before entering the ICP torch. The Nu Plasma II integration time was set to 0.5 s (equivalent to 80 cycles during the 40-s scan). Quality control was ensured by analysing standard apatite samples (including AP-1 and MAD2) after every ten samples⁸¹.

Data availability

Source data are provided with this paper, and deposited in the Figshare data repository (<https://doi.org/10.6084/m9.figshare.26317153>).

References

1. Tyrrell, T. The relative influences of nitrogen and phosphorus on oceanic primary production. *Nature* **400**, 525–531 (1999).
2. Karl, D. M. Microbially mediated transformations of phosphorus in the Sea: new views of an old cycle. *Annu. Rev. Mar. Sci.* **6**, 279–337 (2014).
3. Poulton, S. W. Early phosphorus redigested. *Nat. Geosci.* **10**, 75–76 (2017).
4. Föllmi, K. B. The phosphorus cycle, phosphogenesis and marine phosphate-rich deposits. *Earth Sci. Rev.* **40**, 55–124 (1996).
5. Planavsky, N. J. et al. The evolution of the marine phosphate reservoir. *Nature* **467**, 1088–1090 (2010).
6. Rittenberg, K. C. in *Treatise on Geochemistry* (eds. Holland, H. D. & Turekian, K. K.) 585–643 (Pergamon, 2003).
7. Filippelli, G. M. & Delaney, M. L. Phosphorus geochemistry of equatorial Pacific sediments. *Geochim. Cosmochim. Acta* **60**, 1479–1495 (1996).
8. Hein, R., Gunn, H., Sliter, V. & Benninger, M. Two major Cenozoic episodes of phosphogenesis recorded in Equatorial Pacific seamount deposits. *Paleoceanography* **8**, 293–311 (1993).
9. Jiang, X. et al. Geochemistry and origins of carbonate fluorapatite in seamount Fe–Mn crusts from the Pacific Ocean. *Mar. Geol.* **423**, 1–15 (2020).
10. Zhao, M., Zhang, S., Tarhan, L. G., Reinhard, C. T. & Planavsky, N. The role of calcium in regulating marine phosphorus burial and atmospheric oxygenation. *Nat. Commun.* **11**, 2232 (2020).
11. Benites, M., Hein, J. R., Mizell, K. & Jovane, L. Miocene phosphatization of rocks from the summit of Rio Grande Rise, Southwest Atlantic Ocean. *Paleoceanogr. Paleoclimatol.* **36**, 1–20 (2021).
12. Koschinsky, A., Stascheit, A., Bau, M. & Halbach, P. Effects of phosphatization on the geochemical and mineralogical composition of marine ferromanganese crusts. *Geochim. Cosmochim. Acta* **61**, 4079–4094 (1997).
13. Müller, R. D., Sdrolias, M., Gaina, C. & Roest, W. R. Age, spreading rates, and spreading asymmetry of the world’s ocean crust. *Geophys. Geosyst.* **9**, Q04006 (2008).
14. Josso, P. et al. Improving confidence in ferromanganese crust age models: a composite geochemical approach. *Chem. Geol.* **513**, 108–119 (2019).
15. Klemm, V., Levasseur, S., Frank, M., Hein, J. R. & Halliday, A. N. Osmium isotope stratigraphy of a marine ferromanganese crust. *Earth Planet Sci. Lett.* **238**, 42–48 (2005).
16. Peucker-Ehrenbrink, B. & Ravizza, G. in *The Geologic Time Scale* (eds. Gradstein, F. M., Ogg, J. G., Schmitz, M. D. & Ogg, G. M.) 145–166 (Elsevier, 2012).
17. Chew, D. M., Sylvester, P. J. & Tubrett, M. N. U–Pb and Th–Pb dating of apatite by LA-ICPMS. *Chem. Geol.* **280**, 200–216 (2011).
18. Rochín-Bañaga, H. & Davis, D. W. Insights into U–Th–Pb mobility during diagenesis from laser ablation U–Pb dating of apatite fossils. *Chem. Geol.* **618**, 121290 (2023).
19. Aubineau, J. et al. Geodynamic seawater–sediment porewater evolution of the east central Atlantic Paleogene ocean margin revealed by U–Pb dating of sedimentary phosphates. *Front. Earth Sci.* **10**, 997008 (2022).
20. Li, D. et al. Dating rare earth element enrichment in deep-sea sediments using U–Pb geochronology of bioapatite. *Geology* **51**, 428–433 (2023).
21. O’Sullivan, G. J. et al. Uranium–lead phosphate chronostratigraphy: a proof of concept from the mid-Carboniferous boundary. *Sediment. Geol.* **422**, 1–19 (2021).
22. Rochín-Bañaga, H., Davis, D. W. & Schwennicke, T. First U–Pb dating of fossilized soft tissue using a new approach to paleontological chronometry. *Geology* **49**, 1027–1031 (2021).
23. Ekamparam, A. S. S. & Singh, A. Transformation of calcite to fluorapatite at room temperature: Impact of initial phosphate and fluoride levels. *Geochim. Cosmochim. Acta* **288**, 16–35 (2020).

24. Cappellen, P. V. & Berner, R. A. Fluorapatite crystal growth from modified seawater solutions. *Geochim. Cosmochim. Acta* **55**, 1219–1234 (1991).
25. Piepgras, D. J. & Jacobsen, S. B. The behavior of rare earth elements in seawater: precise determination of variations in the North Pacific water column. *Geochim. Cosmochim. Acta* **56**, 1851–1862 (1992).
26. Klinkhammer, G. P., Elderfield, H., Edmond, J. M. & Mitra, A. Geochemical implications of rare earth element patterns in hydrothermal fluids from mid-ocean ridges. *Geochim. Cosmochim. Acta* **58**, 5105–5113 (1994).
27. Schoene, B. in *Treatise on Geochemistry* Vol. 4, 341–378 (Elsevier, 2014).
28. Stacey, J. S. & Kramers, J. D. Approximation of terrestrial lead isotope evolution by a two-stage model. *Earth Planet Sci. Lett.* **26**, 207–221 (1975).
29. Ben-Israel, M. et al. Late Paleozoic oxygenation of marine environments supported by dolomite U-Pb dating. *Nat. Commun.* **15**, 2892 (2024).
30. Hyeong, K., Kim, J., Yoo, C. M., Moon, J. W. & Seo, I. Cenozoic history of phosphogenesis recorded in the ferromanganese crusts of central and western Pacific seamounts: Implications for deepwater circulation and phosphorus budgets. *Paleogeogr. Paleoclimatol. Paleoecol.* **392**, 293–301 (2013).
31. Aubineau, J. et al. Deciphering the U-Pb dates of sedimentary phosphates: a complex example from the Upper Cretaceous-Lower Paleogene series in northwestern Morocco. *Chem. Geol.* **661**, 122178 (2024).
32. Pufahl, P. K. & Groat, L. A. Sedimentary and igneous phosphate deposits: formation and exploration: an invited paper. *Econ. Geol.* **112**, 483–516 (2017).
33. McArthur, J., Howarth, R. & Shields, G. in *A Geologic Time Scale* Vol. 1, 127–144 (Elsevier, 2012).
34. Li, W. et al. A review of current and emerging approaches for Quaternary marine sediment dating. *Sci. Total Environ.* **780**, 146522 (2021).
35. Mattinson, J. M. Analysis of the relative decay constants of ²³⁵U and ²³⁸U by multi-step CA-TIMS measurements of closed-system natural zircon samples. *Chem. Geol.* **275**, 186–198 (2010).
36. Davis, D. W., Krogh, T. E. & Williams, I. S. Historical development of zircon geochronology. *Rev. Mineral. Geochem.* **53**, 145–181 (2003).
37. Wang, Y. & Fang, N. The relationship between the growth discontinuity of polymetallic crusts and phosphatization events. *HaiyangXuebao* **43**, 102–109 (2021).
38. Hein, J. R. et al. Controls on ferromanganese crust composition and reconnaissance resource potential, Ninetyeast Ridge, Indian Ocean. *Deep-Sea Res. I* **110**, 1–19 (2016).
39. Josso, P., Lusty, P., Chenery, S. & Murton, B. Controls on metal enrichment in ferromanganese crusts: Temporal changes in oceanic metal flux or phosphatisation? *Geochim. Cosmochim. Acta* **308**, 60–74 (2021).
40. Yao, W. & Millero, F. J. Adsorption of phosphate on manganese dioxide in seawater. *Environ. Sci. Technol.* **30**, 536–541 (1996).
41. Fuenzalida, R., Schneider, W., Garcés-Vargas, J., Bravo, L. & Lange, C. Vertical and horizontal extension of the oxygen minimum zone in the eastern South Pacific Ocean. *Deep-Sea Res. II* **56**, 992–1003 (2009).
42. Busecke, J. J. M., Resplandy, L., Ditkovsky, S. J. & John, J. G. Diverging fates of the Pacific Ocean oxygen minimum zone and its core in a warming world. *AGU Adv.* **3**, 1–20 (2022).
43. Schmidtko, S., Stramma, L. & Visbeck, M. Decline in global oceanic oxygen content during the past five decades. *Nature* **542**, 335–339 (2017).
44. Auderset, A. et al. Enhanced ocean oxygenation during Cenozoic warm periods. *Nature* **609**, 77–82 (2022).
45. Brandt, P. et al. On the role of circulation and mixing in the ventilation of oxygen minimum zones with a focus on the eastern tropical North Atlantic. *Biogeosciences* **12**, 489–512 (2015).
46. Song, Y. et al. Dynamic redox and nutrient cycling response to climate forcing in the Mesoproterozoic ocean. *Nat. Commun.* **14**, 6640 (2023).
47. Sánchez, A., Juárez, M., Ortiz-Hernández, M. C. & Domínguez-Samalea, Y. Variability of the oxygen minimum zone associated with primary productivity and hydrographic conditions in the Eastern North Pacific during the last 1200 years. *Deep-Sea Res. I* **186**, 1–7 (2022).
48. Schoepfer, S. D. et al. Total organic carbon, organic phosphorus, and biogenic barium fluxes as proxies for paleomarine productivity. *Earth Sci. Rev.* **149**, 23–52 (2015).
49. Mizell, K., Hein, J. R., Lam, P. J., Koppers, A. A. P. & Staudigel, H. Geographic and oceanographic influences on ferromanganese crust composition along a Pacific Ocean meridional transect, ¹⁴N to ¹⁴S. *Geochem. Geophys. Geosyst.* **21**, 1–19 (2020).
50. Emerson, S. R. & Husteded, S. S. Ocean anoxia and the concentrations of molybdenum and vanadium in seawater. *Mar. Geol.* **34**, 177–196 (1991).
51. Compton, J. et al. in *Marine Authigenesis: From Global to Microbial* Vol. 66, 21–33 (Society for Sedimentary Geology, 2000).
52. Benitez-Nelson, C. R. The biogeochemical cycling of phosphorus in marine systems. *Earth Sci. Rev.* **51**, 109–135 (2000).
53. Paytan, A. & McLaughlin, K. The oceanic phosphorus cycle. *Chem. Rev.* **107**, 563–576 (2007).
54. Filippelli, G. M. & Delaney, M. L. The oceanic phosphorus cycle and continental weathering during the Neogene. *Paleoceanography* **9**, 643–652 (1994).
55. Filippelli, G. M. Phosphate rock formation and marine phosphorus geochemistry: the deep time perspective. *Chemosphere* **84**, 759–766 (2011).
56. Burnett, W. C., Beers, M. J. & Roe, K. K. Growth rates of phosphate nodules from the continental margin off Peru. *Science* **215**, 1616–1618 (1982).
57. Brady, R. X., Maltrud, M. E., Wolfram, P. J., Drake, H. F. & Lovenduski, N. S. The influence of ocean topography on the upwelling of carbon in the Southern Ocean. *Geophys. Res. Lett.* **48**, e2021GL095088 (2021).
58. Goldner, A., Herold, N. & Huber, M. Antarctic glaciation caused ocean circulation changes at the Eocene–Oligocene transition. *Nature* **511**, 574–577 (2014).
59. Diester-Haass, L. & Zahn, R. Eocene–Oligocene transition in the Southern Ocean: history of water mass circulation and biological productivity. *Geology* **24**, 163–166 (1996).
60. Jung, C., Voigt, S., Friedrich, O., Koch, M. C. & Frank, M. Campanian–Maastrichtian ocean circulation in the tropical Pacific. *Paleoceanography* **28**, 562–573 (2013).
61. Jiang, H., Ji, J., Gao, L., Tang, Z. & Ding, Z. Cooling-driven climate change at 12–11 Ma: multiproxy records from a long fluvio-lacustrine sequence at Guyuan, Ningxia, China. *Paleogeogr. Paleoclimatol. Paleoecol.* **265**, 148–158 (2008).
62. Miller, K. G. & Fairbanks, R. G. in *The Carbon Cycle and Atmospheric CO₂: Natural Variations Archean to Present* 469–486 (American Geophysical Union, 1985).
63. Schöllhorn, I. et al. Enhanced upwelling and phosphorite formation in the northeastern Pacific during the late Oligocene: Depositional mechanisms, environmental conditions, and the impact of glacio-eustasy. *Geol. Soc. Am. Bull.* **132**, 687–709 (2020).
64. Nishi, K., Usui, A., Nakasato, Y. & Yasuda, H. Formation age of the dual structure and environmental change recorded in hydrogenetic ferromanganese crusts from Northwest and Central Pacific seamounts. *Ore Geol. Rev.* **87**, 62–70 (2017).

65. Herbert, T. D. et al. Late Miocene global cooling and the rise of modern ecosystems. *Nat. Geosci.* **9**, 843–847 (2016).
66. Filippelli, G. M. Controls on phosphorus concentration and accumulation in oceanic sediments. *Mar. Geol.* **139**, 231–240 (1997).
67. Dickens, G. R. & Owen, R. M. The Latest Miocene–Early Pliocene biogenic bloom: a revised Indian Ocean perspective. *Mar. Geol.* **161**, 75–91 (1999).
68. Gastaldello, M. E. et al. The Late Miocene–Early Pliocene biogenic bloom: an integrated study in the Tasman Sea. *Paleoceanogr. Paleoclimatol.* **38**, e2022PA004565 (2023).
69. Filippelli, G. M. Intensification of the Asian monsoon and a chemical weathering event in the late Miocene–early Pliocene: Implications for late Neogene climate change. *Geology* **25**, 27–30 (1997).
70. Jiang, X. D. et al. Abyssal manganese nodule recording of global cooling and Tibetan Plateau uplift impacts on Asian aridification. *Geophys. Res. Lett.* **49**, 1–10 (2022).
71. Bains, S., Norris, R. D., Corfield, R. M. & Faul, K. L. Termination of global warmth at the Palaeocene/Eocene boundary through productivity feedback. *Nature* **407**, 171–174 (2000).
72. Ma, Z. et al. Carbon sequestration during the Palaeocene–Eocene Thermal Maximum by an efficient biological pump. *Nat. Geosci.* **7**, 382–388 (2014).
73. Nunes, F. & Norris, R. D. Abrupt reversal in ocean overturning during the Palaeocene/Eocene warm period. *Nature* **439**, 60–63 (2006).
74. Soudry, D., Glenn, C. R., Nathan, Y., Segal, I. & Vonderhaar, D. Evolution of Tethyan phosphogenesis along the northern edges of the Arabian–African shield during the Cretaceous–Eocene as deduced from temporal variations of Ca and Nd isotopes and rates of P accumulation. *Earth Sci. Rev.* **78**, 27–57 (2006).
75. Papadomanolaki, N. M., Sluijs, A. & Slomp, C. P. Eutrophication and deoxygenation forcing of marginal marine organic carbon burial during the PETM. *Paleoceanogr. Paleoclimatol.* **37**, e2021PA004232 (2022).
76. Li, J. et al. Reassessment of hydrofluoric acid desilicification in the carius tube digestion technique for Re–Os isotopic determination in geological samples. *Geostand. Geoanal. Res.* **39**, 17–30 (2015).
77. Cohen, A. S. & Waters, F. G. Separation of osmium from geological materials by solvent extraction for analysis by thermal ionisation mass spectrometry. *Anal. Chim. Acta* **332**, 269–275 (1996).
78. Thomson, S. N., Gehrels, G. E., Ruiz, J. & Buchwaldt, R. Routine low-damage apatite U–Pb dating using laser ablation–multicollector–ICPMS. *Geochem. Geophys. Geosyst.* **13**, 2011GC003928 (2012).
79. Chew, D. M., Petrus, J. A. & Kamber, B. S. U–Pb LA–ICPMS dating using accessory mineral standards with variable common Pb. *Chem. Geol.* **363**, 185–199 (2014).
80. Vermeesch, P. IsoplotR: a free and open toolbox for geochronology. *Geosci. Front.* **9**, 1479–1493 (2018).
81. Yang, Y. et al. Sr and Nd isotopic compositions of apatite reference materials used in U–Th–Pb geochronology. *Chem. Geol.* **385**, 35–55 (2014).
82. Seton, M. et al. A Global data set of present-day oceanic crustal age and seafloor spreading parameters. *Geochem. Geophys. Geosyst.* **21**, e2020GC009214 (2020).
83. Moore, T. C., Van Andel, T. H., Sancetta, C. & Pisias, N. G. Cenozoic hiatuses in pelagic sediments. *Micropaleontology* **24**, 113–138 (1978).
84. Westerhold, T. et al. An astronomically dated record of Earth’s climate and its predictability over the last 66 million years. *Science* **369**, 1383–1387 (2020).
85. Voigt, S., Gale, A. S., Jung, C. & Jenkyns, H. C. Global correlation of Upper Campanian – Maastrichtian successions using carbon-isotope stratigraphy: development of a new Maastrichtian time-scale. *Newsl. Stratigr.* **45**, 25–53 (2012).

Acknowledgements

Funding was provided by the National Natural Science Foundation of China (42422306 and 42272066) (D.F.L.), (92262304) (X.M.S.), and Fundamental Research Funds for the Central Universities (23lgbj024) (D.F.L.). D.C. acknowledges support from Science Foundation Ireland through research grants 12/IP/1663, 13/RC/2092 and 13/RC/2092_P2 (iCIRAG Research Centre).

Author contributions

J.Z.P., D.F.L., and X.M.S. conceived and designed the study; J.Z.P. performed the U–Pb dating, major and trace element analyses, and drafted the paper with D.F.L.; S.W.P. aided interpretation and discussion of the results and revised the manuscript; D.C. and G.J.O. provided feedback on the U–Pb dating and helped revise the manuscript. Y.F. provided information on the geological setting.

Competing interests

The authors declare no competing interests.

Additional information

Supplementary information The online version contains supplementary material available at <https://doi.org/10.1038/s41467-024-51598-x>.

Correspondence and requests for materials should be addressed to Dengfeng Li.

Peer review information *Nature Communications* thanks Don Davis, Gabriel Filippelli, Jeremie Aubineau, and the other, anonymous, reviewer(s) for their contribution to the peer review of this work. A peer review file is available.

Reprints and permissions information is available at <http://www.nature.com/reprints>

Publisher’s note Springer Nature remains neutral with regard to jurisdictional claims in published maps and institutional affiliations.

Open Access This article is licensed under a Creative Commons Attribution-NonCommercial-NoDerivatives 4.0 International License, which permits any non-commercial use, sharing, distribution and reproduction in any medium or format, as long as you give appropriate credit to the original author(s) and the source, provide a link to the Creative Commons licence, and indicate if you modified the licensed material. You do not have permission under this licence to share adapted material derived from this article or parts of it. The images or other third party material in this article are included in the article’s Creative Commons licence, unless indicated otherwise in a credit line to the material. If material is not included in the article’s Creative Commons licence and your intended use is not permitted by statutory regulation or exceeds the permitted use, you will need to obtain permission directly from the copyright holder. To view a copy of this licence, visit <http://creativecommons.org/licenses/by-nc-nd/4.0/>.

© The Author(s) 2024